Available online at www.sciencedirect.com

ScienceDirect

Proceedings of the Combustion Institute 38 (2021) 4515–4523

Proceedings of the Combustion Institute

www.elsevier.com/locate/proci

Stability of laminar flames on upper and lower inclined fuel surfaces

R.S.P. Hakes [a,b,*], W. Coenen [b,c], A.L. Sánchez [b], M.J. Gollner [a,d], F.A. Williams [b]

[a] *University of Maryland, College Park, Department of Fire Protection Engineering, College Park, MD 20742, United States*

[b] *Department of Mechanical and Aerospace Engineering, University of California San Diego, La Jolla, CA 92093, United States*

[c] *Dept. Ing. Térmica y de Fluidos, Universidad Carlos III de Madrid, Leganés, Spain*

[d] *Department of Mechanical Engineering, University of California Berkeley, Berkeley, CA 94720, United States*

Received 7 November 2019; accepted 22 June 2020
Available online 1 September 2020

Abstract

Experiments have found substantial morphological differences between buoyancy-driven flames developing on the upper and lower surfaces of inclined burning plates. These differences cannot be explained on the basis of existing analytical solutions of steady semi-infinite flames, which provide identical descriptions for the top and bottom configurations. To investigate the potential role of flame instabilities in the experimentally observed flow differences, a temporal linear stability analysis is performed here. The problem is formulated in the limit of infinitely fast reaction, taking into account the non-unity Lewis number of the fuel vapor. The stability analysis incorporates non-parallel effects of the base flow and considers separately spanwise traveling waves and Görtler-like streamwise vortices. The solution to the stability eigenvalue problem determines the downstream location at which the flow becomes unstable, characterized by a critical value of the relevant Grashof number, whose value varies with the plate inclination angle. The results for the flame formed on the underside of the fuel surface indicate that instabilities emerge farther downstream than they do for a flame developing over the top of the fuel surface, in agreement with experimental observations. Increased buoyancy-induced vorticity production is reasoned to be responsible for the augmented instability tendency of topside flames.

Keywords: Inclined flame; Laminar reacting flows; Buoyancy-driven instability

* Corresponding author at: University of Maryland, College Park, Department of Fire Protection Engineering, College Park, MD 20742, United States.

E-mail address: rhakes@terpmail.umd.edu (R.S.P. Hakes).

https://doi.org/10.1016/j.proci.2020.06.302

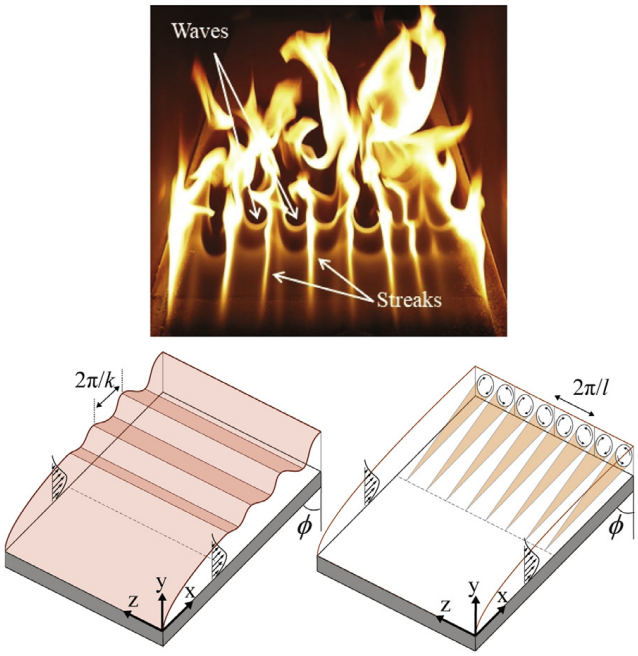

Fig. 1. Top: steady streamwise streaks and traveling spanwise waves are shown over a gas burner used to generate a flame over a surface inclined 70° from the vertical with a very low ∼0.2 m/s crossflow. Bottom: (left) schematic of wave instability, (right) schematic of vortex instability, modified from [16].

1. Introduction

Fires developing on both upper and lower inclined surfaces are commonly encountered in both the built and wildland environments. Inclined flame spread has been a relevant topic of study in the context of fires within enclosed spaces [1] and larger-scale wildland fires. While some work has investigated flame spread on the upper side of an inclined surface, flame spread along the lower side of an inclined surface, relevant to fires in attics and inclined ceilings, has received less attention. Experiments [2,3] have observed that the structure of a flame that forms on the topside of an inclined fuel surface is distinctly different from a flame that forms on the underside of the fuel surface. A majority of studies on topside flame spread have assumed the flame structure to be essentially two-dimensional; however, recent studies have shown that flames often form unique three-dimensional structures driven by instabilities in the flow, such as spanwise waves and streamwise streaks, which may contribute to augmented heat transfer, resulting in faster flame spread [4,5]. Both types of instabilities are visible in the image of a flame developing over an inclined burner shown in Fig. 1.

A number of relevant studies on topside inclined flame spread are summarized in [6]. Previous numerical studies describe the flame shape, velocity and temperature fields, and the mass burning rate [7,8]. Studies on upward flame spread have developed simplified theoretical models for steady laminar vertical flames [9]. Although no previous studies have addressed the stability of these flows, a similar problem, the structure and stability of the flow that develops over the topside of an inclined heated plate, has been studied extensively over the last fifty years. Early experiments [10,11] and theoretical analyses [12,13] found two modes of instability, a vortex instability, characterized by stationary Görtler-type streamwise vortices, and a wave instability, characterized by Tollmein-Schlichting spanwise traveling waves. As seen for flames in Fig. 1, these instabilities develop to form streaks and waves of finite amplitude that interact in a nonlinear fashion, eventually leading to a transition to turbulence. Early analytical studies [12,13] found that the flow became more unstable as the angle of inclination ϕ was increased from the vertical. For small values of ϕ below a critical value of $\phi \simeq$ 14–17°, the wave mode was found to be dominant; for larger angles, the vortex mode was found to be dominant. While these early studies used the Boussinesq approximation, recent analyses have considered non-Boussinesq effects in describing the structure [14] and stability [15] of the the flow over an inclined heated plate. The former [14] found that the flows over the topside and underside of an inclined heated plate are identical. The latter [15] found that, for the topside configuration, the flow becomes increasingly unstable as the value of the plate-to-ambient temperature ratio is increased. When the ratio is increased above 1.8, the wave mode becomes dominant for

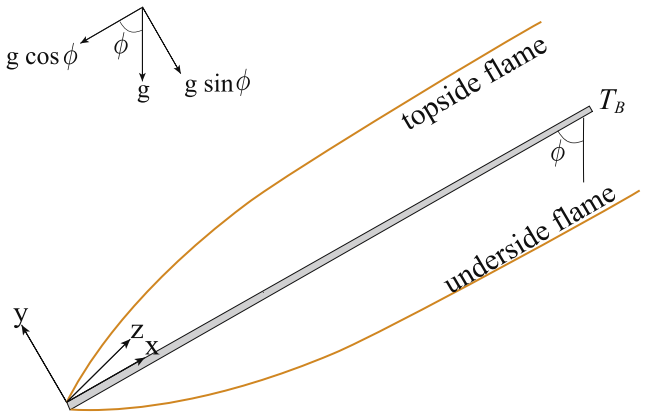

Fig. 2. A schematic representation of the flame forming over the topside or the underside of an inclined fuel surface. The coordinate system is indicated for a topside flame; for the underside flame, the y-coordinate points in the opposite, downward, direction.

all ϕ. The present work extends these previous non-Boussinesq studies to cases in which density differences are due to a diffusion flame burning the fuel vaporized from a semi-infinite inclined surface with the oxygen in the surrounding air atmosphere. In particular, we investigate whether the instabilities in the flow can account for the observed experimental differences between topside and underside flames.

2. General formulation

A description of a laminar flame burning over a semi-infinite fuel surface inclined at an angle ϕ from the vertical, shown in Fig. 2, must consider the continuity and momentum equations

$$\frac{\partial \rho}{\partial t} + \nabla \cdot (\rho \mathbf{v}) = 0, \tag{1}$$

$$\frac{\partial \mathbf{v}}{\partial t} + \mathbf{v} \cdot \nabla \mathbf{v} = -\frac{\nabla p}{\rho} + \frac{1}{\rho} \nabla \cdot [\mu(\nabla \mathbf{v} + \nabla \mathbf{v}^T)] + \left(1 - \frac{\rho_\infty}{\rho}\right)\mathbf{g}, \tag{2}$$

where ρ, μ, and $\mathbf{v}$ represent the dimensional density, viscosity, and velocity of the gas, and the subscript ∞ denotes ambient air properties. The flow is characterized by small values of the associated Mach number, so that the spatial variations of the pressure are much smaller than the ambient value. In (2), p denotes the sum of the pressure difference from the ambient hydrostatic value and the isotropic component of the stress tensor. Cartesian coordinates are used to describe the flow, including the streamwise coordinate x, the transverse coordinate y, and the spanwise coordinate z, with corresponding velocity components $\mathbf{v} = (v_x, v_y, v_z)$. The gravity vector is $\mathbf{g} = -g\cos\phi\, \bar{e}_x - g\sin\phi\, \bar{e}_y$, where g is the magnitude of the gravitational acceleration and the $\bar{e}$'s are unit vectors in the subscript direction. The differences between the topside and underside flame are a result of the transverse gravitational acceleration $-g\sin\phi$, negative on the topside ($\phi > 0$) and positive on the underside ($\phi < 0$).

The reaction between the fuel and the oxygen in the air is taken to occur according to a global irreversible reaction $\mathrm{F} + s\mathrm{O}_2 \longrightarrow (1+s)\mathrm{P} + q'$, where s and q' are the mass of oxygen consumed and the amount of heat released per unit mass of fuel burnt, respectively. These thermochemical parameters appear in the equations below as $S = s/Y_{O_2 A}$ and $q = q'/(c_p T_\infty)$, where $Y_{O_2 A} \simeq 0.232$ is the ambient oxygen mass fraction, c_p is the specific heat at constant pressure, assumed to be constant, and T is the temperature. Values of S, the mass of air needed to burn a unit mass of fuel vapor, are of order $S \sim 6$ for alcohol fuels and $S \sim 15$ for alkanes, while the ratio q/S is approximately $q/S \simeq 7$ for all fuels of interest.

In the limit of infinitely fast reaction considered here, the flame appears as an infinitesimally thin surface separating an oxygen-free fuel region from the surrounding fuel-free air. Following [16,17] the problem is formulated in terms of coupling functions that account for non-unity values of the Lewis number of the fuel vapor Le_F. The description includes two different mixture fractions

$$Z = \frac{SY_F - Y_O + 1}{S+1} \quad \text{and} \quad \tilde{Z} = \frac{SY_F/Le_F - Y_O + 1}{S/Le_F + 1} \tag{3}$$

and a modified enthalpy

$$\xi = \frac{T/T_\infty - 1 + (q/S)(Y_O - 1)}{T_B/T_\infty - 1 - q/S} \tag{4}$$

with associated transport equations

$$\rho \frac{\partial Z}{\partial t} + \rho \mathbf{v} \cdot \nabla Z = \frac{1}{Le} \nabla \cdot (\rho D_T \nabla \tilde{Z}) \tag{5}$$

and

$$\rho \frac{\partial \xi}{\partial t} + \rho \mathbf{v} \cdot \nabla \xi = \nabla \cdot (\rho D_T \nabla \xi). \tag{6}$$

Here Y_F and $Y_O = Y_{O_2}/Y_{O_2 A}$ are, respectively, the mass fraction of the fuel vapor and the normalized mass fraction of the oxygen, $Le = (S+1)/(S/Le_F + 1)$ is an effective Lewis number, D_T is the thermal diffusivity of the gas mixture, and T_B is the boiling temperature of the fuel. As discussed in [18], the effect of heat losses by radiation, which has been neglected in writing (6), could be incorporated approximately in the description by lowering the value of q.

The conservation equations are supplemented by the equation of state written in the low-Mach number form

$$\frac{\rho}{\rho_\infty}\frac{T}{T_\infty} = \left[Y_F\left(\frac{W_A}{W_F} - 1\right) + 1\right], \tag{7}$$

which accounts for the large density variations associated with the presence of the fuel vapor, with W_F and W_A representing the molecular masses of the fuel and air, respectively. The presumed power law

$$\frac{\mu}{\mu_\infty} = \frac{\rho}{\rho_\infty}\frac{D_T}{D_{T,\infty}} = \left(\frac{T}{T_\infty}\right)^\sigma \tag{8}$$

with $\sigma = 0.7$ is used in the numerical integration for the temperature dependence of the transport properties.

Vaporization of the liquid fuel is taken to occur at the boiling temperature of the fuel with latent heat of vaporization L_v. A dimensionless heat of vaporization $l_v = [L_v + c_l(T_B - T_\infty)]/(c_p T_\infty)$ is introduced to account for the energy required to raise the temperature of the liquid fuel, with specific heat c_l, from T_∞ to T_B.

The equilibrium condition associated with the infinitely fast reaction limit $Y_F Y_O = 0$ is used to solve (1), (2), (5), and (6) supplemented by (7) and (8). Both reactants reach the flame with zero mass fraction, so that the flame values of the mixture fraction variables are $Z = Z_S = 1/(S+1)$ and $\tilde{Z} = \tilde{Z}_S = 1/(S/Le_F + 1)$. Using the equilibrium condition and the definitions (3) and (4) provides

$$Y_O = 0, \quad Y_F = \frac{Z - Z_S}{1 - Z_S} = \frac{\tilde{Z} - \tilde{Z}_S}{1 - \tilde{Z}_S}, \quad \text{and}$$
$$T/T_\infty - 1 = (T_B/T_\infty - 1)\xi + (q/S)(1 - \xi) \tag{9}$$

on the fuel side of the flame sheet, where $\tilde{Z} \geq \tilde{Z}_S$, and

$$Y_F = 0, \quad 1 - Y_O = Z/Z_S = \tilde{Z}/\tilde{Z}_S, \quad \text{and}$$
$$T/T_\infty - 1 = (T_B/T_\infty - 1)\xi + (q/S)\left(\tilde{Z}/\tilde{Z}_S - \xi\right) \tag{10}$$

on the air side of the flame sheet, where $\tilde{Z} \leq \tilde{Z}_S$. Eqs. (9) and (10) give piecewise linear relations for the evaluation of Y_F, Y_O, and Z in terms of $\tilde{Z}$, and of T in terms of $\tilde{Z}$ and ξ.

To complete the problem, boundary conditions are given in the farfield

$$v_x = v_y = p = \tilde{Z} = \xi = 0 \quad \text{as} \quad (x^2 + y^2) \to \infty \quad \text{for} \quad y \neq 0 \tag{11}$$

and at the fuel surface

$$\left.\begin{aligned} v_x = \xi - 1 = 0 \\ -\rho D_T \frac{\partial \xi}{\partial y} = \alpha \rho v_y \\ -\rho D_T \frac{\partial \tilde{Z}}{\partial y} = Le_F\ \rho v_y (1 - \tilde{Z}) \end{aligned}\right\} \text{at } y = 0 \text{ for } x > 0, \tag{12}$$

where $\alpha = l_v/[(q/S) + 1 - T_B/T_\infty]$. The condition $\xi = 1$ corresponds to $T = T_B$ at the fuel surface, where $Y_O = 0$.

3. Self-similar formulation for steady flames

Interest here lies in the slender boundary layer that develops over the fuel surface at distances from the plate leading edge x that are large compared with the size $\delta_{NS} = [\nu_\infty^2/(g\cos\phi)]$ of the so-called Navier-Stokes region [14]. An order-of-magnitude analysis of the continuity and momentum equations provides the estimates $\delta = (\nu_\infty^2 x)^{1/4}(g\cos\phi)^{-1/4}$, $u_c = (xg\cos\phi)^{1/2}$, and $v_c = (\nu_\infty^2\ g\cos\phi/x)^{1/4}$ for the variation with x of the boundary-layer thickness δ and the associated streamwise and transverse velocity components, u_c and v_c. These values are used in writing dimensionless conservation equations for the base flow. The solution is expressed in terms of the self-similar coordinate $\eta = y\,(\nu_\infty^2 x/g\cos\phi)^{-1/4}$, the dimensionless temperature $\Theta(\eta) = T/T_\infty$, and the stream function $\psi = \rho_\infty(\nu_\infty^2 x^3\ g\cos\phi)^{1/4} F(\eta)$ related to velocity by

$$U = v_x/(xg\cos\phi)^{1/2} = F'/\bar{\rho} \tag{13}$$

$$V = v_y/(\nu_\infty^2\ g\cos\phi/x)^{1/4} = \tfrac{1}{4}(\eta F' - 3F)/\bar{\rho} \tag{14}$$

where $\bar{\rho} = \rho/\rho_\infty$ and the prime is used to denote differentiation with respect to η. The problem reduces to the integration of (2), (5), and (6) written in the self-similar form

$$[\Theta^\sigma (F'/\bar{\rho})']' + \tfrac{3}{4}F(F'/\bar{\rho})' - \tfrac{1}{2}(F')^2/\bar{\rho} + 1 - \bar{\rho} = 0 \tag{15}$$

$$(\Theta^\sigma \tilde{Z}')' + \tfrac{3}{4} LePrF\tilde{Z}' = 0 \tag{16}$$

$$(\Theta^\sigma \xi')' + \tfrac{3}{4} PrF\xi' = 0 \tag{17}$$

with boundary conditions $F' = \tilde{Z} = \xi = 0$ as $\eta \to \infty$ and $F' = \xi - 1 = 0$ and $3/4 Pr\Theta_B^{-\sigma} F = \xi'/\alpha = \tilde{Z}'[Le_F(1 - \tilde{Z})]^{-1}$ at $\eta = 0$, corresponding to (11) and (12).

Table 1
Fuel properties used in numerical integration.

	W_F/W_A	l_v	θ_B	Le_F	q/S	S
Methanol	1.1	2.87	1.12	1.2	7.7	6.47
Ethanol	1.59	2.29	1.17	1.4	7.35	8.98
Heptane	3.46	1.14	1.24	1.8	7.0	15.2

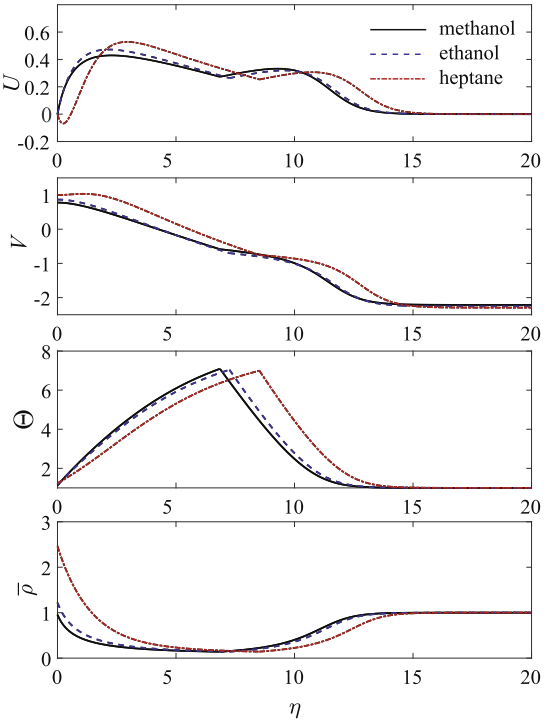

Fig. 3. From top to bottom: dimensionless measures of streamwise and transverse velocity, following (13) and (14), dimensionless temperature, and dimensionless density as a function of η.

The solution to (15)–(17), independent of the inclination angle, is complicated by discontinuities in the derivatives of the density and temperature at the flame. In order to overcome this difficulty, the problem is split into two domains separated by the flame surface $\eta = \eta_s$. In each domain, the system of ordinary differential equations is solved using a Chebyshev spectral collocation method. The split domain introduces unknown boundary conditions at η_s, which are solved iteratively using a standard Newton-Raphson algorithm. The self-similar base flow was solved using the transport, thermochemical, and vaporization properties of methanol, ethanol, and heptane, given in Table 1.

4. Solution for the steady base flow

Results for the base flow, including dimensionless profiles of velocity, temperature, and density, are shown in Fig. 3. The profiles, which differ considerably from those obtained previously for the heated plate [14], exhibit discontinuities in slope at the flame, which is located at $\eta_s = 6.9$, 7.3, and 8.5 for methanol, ethanol, and heptane, respectively. Perhaps unexpectedly, differences in flame location between different fuels remain relatively small, a result that can be attributed to cancellation of competing effects. The large Le_F of heptane indicates that it is less diffusive than the alcohols, which would result in a flame that lies closer to the plate. On the other hand, the amount of air needed to oxidize a unit mass of heptane S is much larger than the corresponding values for methanol or ethanol (shown in Table 1), which would cause the heptane flame to lie farther from the plate than the alcohol flames. The two effects tend to cancel each other, with the result that the heptane flame lies only slightly farther from the plate than do the alcohol flames. The most significant differences between the base flow of the heptane and alcohol flames are found in the density profiles, with the heptane flame exhibiting larger density differences than the alcohol flames, a result of the disparities in molecular weight. Although radiation is generally found to be small in comparison to convection for small-scale laminar flames [19,20], future work should consider the effects of radiation, which may be larger for heptane. The selection of a smaller value of the heat release parameter q may lead to lower and more realistic flame temperatures [18].

5. Formulation of the linear stability analysis

The temporal linear stability of the flow to wave and vortex modes is investigated by introducing perturbations into (1), (2), (5), and (6) at a point $x = x_0$ some distance from the leading edge of the plate, such that $x_0 \gg \delta_{NS}$. The characteristic values $\delta_0 = [(\nu_\infty^2 x_0)/(g\cos\phi)]^{1/4}$ and $u_0 = (x_0 g\cos\phi)^{1/2}$ are used as length and velocity scales to nondimensionalize the problem with δ_0/u_0 correspondingly used as the time scale. Density and transport properties are scaled with their relevant ambient values. The self-similar profiles and their corresponding derivatives (denoted by a prime) will be used to evaluate the base flow. The ratio of the streamwise distance to the local boundary-layer thickness defines the Grashof number $Gr = x_0/\delta_0 = (x_0^3 g\cos\phi)^{1/4}\nu_\infty^{-1/2} \gg 1$, the relevant bifurcation parameter in the stability study. The linearized equations for the quasi-parallel flow are expressed in terms of normal-mode perturbations

$$e^{i(k\tilde{x}+l\tilde{z}-\omega\tilde{t})}\left[\hat{\rho}, \hat{\mu}, \hat{p}, \hat{v}_x, \hat{v}_y, \hat{v}_z, \hat{Z}, \hat{\tilde{Z}}, \hat{\xi}\right](\tilde{y}), \tag{18}$$

involving the dimensionless variables $\tilde{x} = (x - x_0)/\delta_0$, $\tilde{y} = y/\delta_0$, $\tilde{z} = z/\delta_0$, and $\tilde{t} = t/(\delta_0/u_0)$. The coefficients k and l in the exponential factor are the dimensionless streamwise and spanwise wave numbers, while $\omega = \omega_r + i\omega_i$ defines the frequency ω_r and the growth rate ω_i of the perturbations. We an-

ticipate two modes of instability, a wave instability for which $l = 0$ and a vortex instability for which $k = 0$ and $\omega_r = 0$.

As in previous work [15], the slow streamwise variation of the base flow and molecular transport effects, terms in the equations not involving Gr, are accounted for when writing the linearized equations, as is needed for increased accuracy when the Grashof number is not large. The introduction of normal modes into the linearized equations leads to the following eigenvalue problem

$$\mathrm{i}Gr(kU-\omega)\hat{\rho}+[U/2-(\tilde{y}/4)U'+\mathrm{D}V]\hat{\rho}+[\mathrm{i}Grk\bar{\rho} -(\tilde{y}/4)\bar{\rho}']\hat{v}_x+\mathrm{i}Gr(\mathrm{D}\bar{\rho})\hat{v}_y+\mathrm{i}Grl\bar{\rho}\hat{v}_z=0, \tag{19}$$

$$[U(U/2-(\tilde{y}/4)U')+U'V+1]\hat{\rho}-(\mathrm{D}U')\hat{\mu}+\mathrm{i}Grk\hat{p} +[\mathrm{i}Gr\bar{\rho}(kU-\omega)+U/2-(\tilde{y}/4)U'+\Theta^{\sigma}(2k^2+l^2)]\hat{v}_x +[\bar{\rho}V\mathrm{D}-\mathrm{D}(\Theta^{\sigma}\mathrm{D})]\hat{v}_x+[\mathrm{i}Gr\bar{\rho}U'+k(\mathrm{D}\Theta^{\sigma})]\hat{v}_y +kl\Theta^{\sigma}\hat{v}_z=0, \tag{20}$$

$$Gr\mathrm{D}\hat{p}+\tan\phi\hat{\rho}-\mathrm{i}kU'\hat{\mu}-\mathrm{i}k\Theta^{\sigma}\mathrm{D}\hat{v}_x+[Gr\bar{\rho}(\omega-kU) +\mathrm{i}\Theta^{\sigma}(k^2+l^2)]\hat{v}_y+\mathrm{i}[\bar{\rho}(\mathrm{D}V)-2\mathrm{D}(\Theta^{\sigma}\mathrm{D})]\hat{v}_y -\mathrm{i}l\Theta^{\sigma}\mathrm{D}\hat{v}_z=0, \tag{21}$$

$$\mathrm{i}Grl\hat{p}+kl\Theta^{\sigma}\hat{v}_x+l(\mathrm{D}\Theta^{\sigma})\hat{v}_y+[\mathrm{i}Gr\bar{\rho}(kU-\omega) +\Theta^{\sigma}(k^2+2l^2)]\hat{v}_z+[\bar{\rho}V\mathrm{D}-\mathrm{D}(\Theta^{\sigma}\mathrm{D})]\hat{v}_z=0, \tag{22}$$

$$\overline{Z}'[V-(\tilde{y}/4)U]\hat{\rho}-(LePr)^{-1}(\mathrm{D}\tilde{Z}')\hat{\mu}-(\tilde{y}/4)\bar{\rho}Z'\hat{v}_x +\mathrm{i}Gr\bar{\rho}Z'\hat{v}_y+[\mathrm{i}Gr\bar{\rho}(kU-\omega)+\bar{\rho}V\mathrm{D}]\hat{Z} +(LePr)^{-1}[\Theta^{\sigma}(k^2+l^2)-\mathrm{D}(\Theta^{\sigma}\mathrm{D})]\hat{\tilde{Z}}=0, \tag{23}$$

$$\overline{\xi}'[V-(\tilde{y}/4)U]\hat{\rho}-Pr^{-1}(\mathrm{D}\overline{\xi}')\hat{\mu}-(\tilde{y}/4)\bar{\rho}\xi'\hat{v}_x +\mathrm{i}Gr\bar{\rho}\xi'\hat{v}_y+[\mathrm{i}Gr\bar{\rho}(kU-\omega)+\bar{\rho}V\mathrm{D}]\hat{\xi} +Pr^{-1}[\Theta^{\sigma}(k^2+l^2)-\mathrm{D}(\Theta^{\sigma}\mathrm{D})]\hat{\xi}=0, \tag{24}$$

with homogeneous boundary conditions in the farfield

$$\hat{p}=\hat{v}_x=\hat{v}_y=\hat{v}_z=\hat{\tilde{Z}}=\hat{\xi}=0 \quad \text{as} \quad \tilde{y}\to\infty \tag{25}$$

and on the vaporizing surface $\tilde{y}=0$

$$\hat{v}_x=\hat{v}_z=\hat{\xi}=0, \tag{26}$$

$$(1-\overline{\tilde{Z}})(V\hat{\rho}+\mathrm{i}Gr\bar{\rho}\hat{v}_y)-\bar{\rho}V\hat{\tilde{Z}} +(Le_FPr)^{-1}[(\Theta^{\sigma}\mathrm{D})\hat{\tilde{Z}}+\overline{\tilde{Z}}'\hat{\mu}]=0, \quad \text{and} \tag{27}$$

$$\alpha(\hat{\rho}V+\mathrm{i}Gr\bar{\rho}\hat{v}_y)+Pr^{-1}[(\Theta^{\sigma}\mathrm{D})\hat{\xi}+\overline{\xi}'\hat{\mu}]=0 \tag{28}$$

where the base-flow functions are evaluated at $\tilde{y}$, and symbols immediately following D are to be multiplied by the eigenfunction prior to differentiation, as in [15].

The stability Eqs. (19)–(24), with $\hat{\rho}$, $\hat{\mu}$, and $\hat{Z}$ written as functions of $\hat{\xi}$ and $\hat{\tilde{Z}}$ using (7)–(10), are discretized using a Chebyshev spectral collocation method. Upon discretization, the stability equations are written as the discrete generalized eigenvalue problem $Aq=\omega Bq$ for the complex eigenvalue ω, where $q=(\hat{p},\hat{v}_x,\hat{v}_y,\hat{v}_z,\hat{\tilde{Z}},\hat{\xi})$ and A and B are the discretized matrices associated with the stability equations that are dependent on k, l, Gr, and the base flow.

6. Results of the linear stability analysis

All modes are found to be stable at sufficiently small values of the Grashof number. Above a critical value of the Grashof number Gr_C, one of these modes begins to exhibit a positive growth rate. The characteristics of that mode and the Gr_C at which it becomes unstable determine the nature of the instability that initially develops and the position along the inclined plate at which that development occurs, for any given ϕ. The numerical solution can be simplified for the vortex mode because $k=\omega_r=0$ allows $\tan\phi$ to be scaled out of the normal-mode equations by setting

$$(\breve{Gr},\breve{\mathbf{v}},\breve{\rho},\breve{\mu},\breve{Z},\breve{\tilde{Z}},\breve{\xi}) =(Gr,\hat{\mathbf{v}},\hat{\rho},\hat{\mu},\hat{Z},\hat{\tilde{Z}},\hat{\xi})\tan\phi, \quad \breve{p}=\hat{p}/\tan\phi. \tag{29}$$

As a result, the vortex mode can be solved independently of ϕ to determine the critical value $\breve{Gr}_C$ of $\breve{Gr}$, which in turn provides the expression

$$Gr_C=\breve{Gr}_C/\tan\phi \tag{30}$$

for the inclination dependence of the vortex mode. This type of simplification is unavailable for the wave mode.

The linearized normal-mode equations are solved for a given wave number and Grashof number to determine the growth rate of the instability. As Gr is increased, the flame eventually becomes unstable for one wave number; as it is further increased, it becomes unstable for a larger range of wave numbers. Figure 4 shows this trend for a vertical laminar heptane flame, where the wave mode is dominant. For low Gr, the flame is stable for all wave numbers. At $Gr_C=3.9$, the flame becomes unstable for $k=0.29$. As Gr is further increased, a larger range of k becomes unstable.

The dependence on inclination angle of the critical Grashof number of the wave and vortex instability modes is shown in Fig. 5 for both the topside (right) and underside (left) flame. The results for the vortex mode correspond to the prediction (30), with $\breve{Gr}_C=3.33$ and 26.48 for the topside and underside, respectively. Since the critical value of the Grashof number diverges as $\phi\to 0$, the flame for the vertical

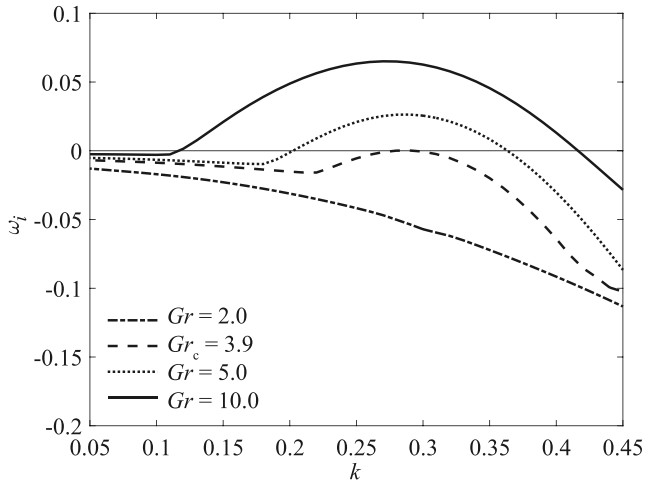

Fig. 4. Growth rate of the wave-mode instability for a heptane flame as a function of wave number at $\phi = 0$ (vertical) for increasing Gr. Below $\omega_i = 0$, the flame is stable; for values of $\omega_i > 0$, the flame is unstable for the corresponding wave numbers.

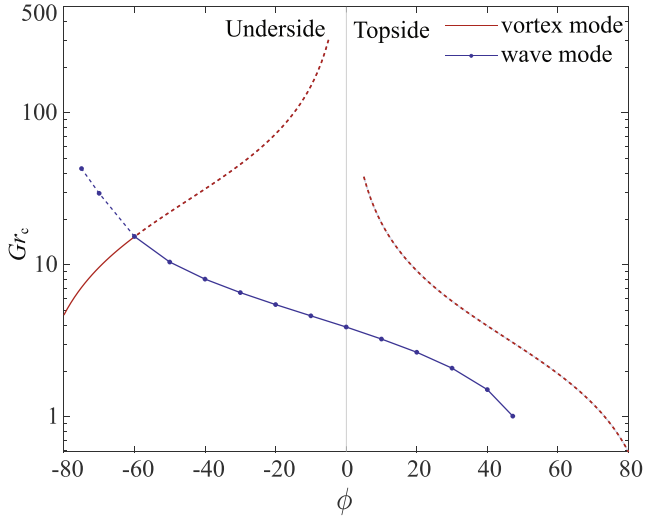

Fig. 5. Variation of Gr_C with inclination angle for the wave mode and vortex mode for a topside heptane flame and an underside heptane flame. For the vortex mode, $\check{G}r_C = 3.33$ and 26.48 for the topside and underside, respectively.

orientation is subject only to the wave-mode instability, with $Gr_C = 3.9$ for $\phi = 0^\circ$. The vortex mode curves are plotted only for angles below $\phi = 80^\circ$, above which the surface is near-horizontal. For the flame in the horizontal orientation, the pressure differences across the boundary layer, negligible in the self-similar inclined analysis, become significant.

For the topside flame, the wave-mode results can be calculated only as far as $\phi = 47.22^\circ$, for which Gr_C becomes exactly $Gr_C = 1$. For larger values of ϕ, the numerical analysis was unable to find stable conditions, regardless of the value of Gr. This breakdown is attributed to the limitations of the slender-flow analysis, in that, for $Gr < 1$, the terms of order Gr^{-2} and higher that were discarded in writing the stability problem become larger than those retained.

Figure 5 indicates that the underside flame is clearly more stable than the topside flame, for both instability modes. The wave mode is the first bifurcation for the topside and also for most values of ϕ of the underside. While Gr_C decreases monotonically with increasing $|\phi|$ for the vortex mode, the value of Gr_C for the wave mode decreases for the topside flames, but increases for underside flames. Unlike previous work on the inclined heated plate [15], the topside flame exhibits no crossover angle, at which the dominant instability switches modes. A crossover angle does occur, however, for the underside flame at $\phi = -60^\circ$; at angles closer to the horizontal, the vortex mode dominates.

7. Discussion

The results presented for the stability of the flame may be compared with the results for the stability of the flow over an inclined heated plate [15]. In that analysis, the flow is found to become increasingly unstable as the plate temperature increases. For example, at an inclination angle of 10° from the vertical, as the plate-to-ambient temperature ratio was increased from 1.03 to 3.0, the Gr_C dropped from approximately 75 to 15. The study did not consider larger temperature ratios. Nonetheless, the trend indicates that the Gr_C for larger temperature ratios would be of the same order of magnitude as that found here for the stability of the inclined topside flame.

The differences in the stability of the flame forming on the topside as opposed to the underside of an inclined fuel surface can be investigated by considering the physical mechanisms governing the growth of instabilities. The vortex mode instability is similar to the Rayleigh-Bénard instability; the flame becomes unstable because of perturbations resulting from density differences. This effect is larger on the topside than on the underside because above the flame there is a large unstable region, similar to the situation found for the hot plate, while the flame on the underside possesses only a thin unstable region, confined between the flame and the fuel surface.

The wave instability is associated with vorticity production in the spanwise direction resulting from either buoyancy-induced or baroclinic-torque effects. The magnitude of the vorticity production and whether it enhances or suppresses a perturbation influences the stability of the flame. The equation for the vorticity perturbation Ω_z has two production terms, the baroclinic torque $\Gamma_b = -\nabla(1/\bar{\rho}) \times \nabla p$, and the buoyancy-induced torque $\Gamma_g = -\nabla(\rho/\bar{\rho}^2) \times (\bar{e}_x + \tan\phi \bar{e}_y)$, where $\bar{e}_x$ and $\bar{e}_y$ are the unit vectors in the x and y directions, respectively. In normal mode form, the vorticity can be written as $\hat{\Omega}_z = -k\hat{v}_y - \mathrm{D}\hat{v}_x$, and the production terms as $\hat{\Gamma}_b = -(1/\bar{\rho}^2)(\mathrm{i}k\bar{\rho}'\hat{p} + Gr^{-1}\tilde{y}\bar{\rho}'\mathrm{D}\hat{p}/4)$ and $\hat{\Gamma}_g = -(Gr^{-1}/\bar{\rho}^2)[(\mathrm{i}k\tan\phi + 2\bar{\rho}'/\bar{\rho})\hat{\rho} - \mathrm{D}\hat{\rho}]$. The effects of buoyancy-induced vorticity are dominated by the sign of $\tan\phi$. As the fuel surface is tilted from the vertical, the topside becomes incrementally less stable, while the underside stabilizes. The stabilizing and de-stabilizing contributions of both baroclinic and buoyancy-induced torque should be analyzed in future work following the method presented in [21].

8. Conclusions and future work

The results of the linear stability analysis indicate that instabilities in the flame may contribute to some of the morphological differences observed between flames forming on the topside and the underside of an inclined fuel surface. The underside flame is seen to be more stable than the topside flame, which is consistent with experimental observations. Nonetheless, the quantitative results must be taken with caution because of the resulting order-unity values of Gr_C obtained for the topside flame. For a more accurate quantification of the flame stability, a model would need to take into account the spatial development of the instabilities. The present analysis is a first step in understanding the differences between topside and underside flames. Future work will compare results from the theoretical analysis with experiments to test the predictions and assess the validity of the underlying assumptions. New experiments are in progress because of the paucity of experimental results. It is possible that the instability may help to trigger liftoff of the flame from the top surface of the plate, a phenomenon that has been seen experimentally. Comparisons of instability predictions with experimentally measured liftoff conditions can ultimately indicate how helpful the stability analyses can be in estimating when liftoff may occur.

Declaration of Competing Interest

The authors declare that they have no known competing financial interests or personal relationships that could have appeared to influence the work reported in this paper.

Acknowledgments

The authors would like to thank Mike Heck and Mahdi Tlemsani for their assistance with laboratory experiments. This material is based upon work supported by the National Science Foundation Graduate Research Fellowship Program under Grant #DGE 1322106 and the Clark Doctoral Fellows Program at the University of Maryland. MJG acknowledges support from National Science Foundation award #1554026. WC and ALS acknowledge support from National Science Foundation grant #1916979.

References

[1] D. Drysdale, A. Macmillan, *Fire Saf. J.* 18 (1992) 75–82.
[2] M. Gollner, X. Huang, J. Cobian, A. Rangwala, F. Williams, *Proc. Combust. Inst.* 34 (2013) 2531–2538.
[3] X. Huang, M. Gollner, *Fire Saf. Sci.* 11 (2014) 222–233.
[4] M. Finney, J. Cohen, J. Forthofer, S. McAllister, M. Gollner, D. Gorham, K. Saito, N. Akafuah, B. Adam, J. English, *Proc. Natl. Acad. Sci. USA* 112 (32) (2015) 9833–9838.

[5] C. Miller, W. Tang, M. Finney, S. McAllister, J. Forthofer, M. Gollner, *Combust. Flame* 181 (2017) 123–135.
[6] M. Gollner, C. Miller, W. Tang, A. Singh, *Fire Saf. J.* 91 (2017) 68–78.
[7] S. Ali, V. Raghavan, A. Rangwala, *Combust. Theor. Model.* 14 (2010) 495–518.
[8] S. Ali, V. Raghavan, A. Rangwala, *Fire Saf. J.* 49 (2012) 67–78.
[9] A. Fernandez-Pello, *Combust. Flame* 31 (1978) 135–148.
[10] E. Sparrow, R. Husar, *J. Fluid Mech.* 37 (1969) 251–255.
[11] J. Lloyd, E. Sparrow, *J Fluid Mech* 42 (3) (1970) 465–470.
[12] S. Haaland, S. Sparrow, *Int. J. Heat Mass Transf.* 16 (12) (1973) 2355–2367.
[13] S. Haaland, S. Sparrow, *J. Heat Transf.* 95 (3) (1973) 405–407.
[14] M. Gollner, A.L. Sánchez, F. Williams, *J. Fluid Mech.* 732 (2013) 304–315.
[15] P. Rajamanickam, W. Coenen, A.L. Sánchez, *Int. J. Heat Mass Transf.* 109 (2017) 949–957.
[16] D. Gómez Lendínez, *Stability of Laminar Jets and Clarke-Riley Flames*, Universidad Carlos III de Madrid, 2018 Ph.D. thesis.
[17] A. Liñán, M. Vera, A.L. Sánchez, *Annu. Rev. Fluid Mech.* 47 (2015) 293–314.
[18] D. Moreno-Boza, W. Coenen, J. Carpio, A.L. Sánchez, F. Williams, *Combust. Flame* 192 (2018) 426–438.
[19] T. Ahmad, E. Groff, G. Faeth, Fire-Induced Plumes Along a Vertical Wall: Part II: the Laminar Combusting Region, *Technical Report*, Mechanical Engineering Department, The Pennsylvania State University, July 1977.
[20] P. Blackshear, K. Murty, *Proc. Combust. Inst.* 11 (1967) 545–552.
[21] L. Lesshafft, P. Huerre, *Phys. Fluids* 19 (2007).